AN ELECTROCHEMICAL EVALUATION OF NITROGEN-DOPED CARBONS AS ANODES FOR LITHIUM ION BATTERIES

A. Gomez-Martin[a*], J. Martinez-Fernandez[a], Mirco Ruttert[b], Martin Winter[b, c], Tobias Placke[b], J. Ramirez-Rico[a, *]

[a] Dpto. Física de la Materia Condensada and Instituto de Ciencia de Materiales de Sevilla, Universidad de Sevilla – CSIC, Avda. Reina Mercedes SN, 41012 Sevilla, Spain

[b] University of Münster, MEET Battery Research Center, Institute of Physical Chemistry, Corrensstraße 46, 48149 Münster, Germany

[c] Helmholtz Institute Münster, IEK-12, Forschungszentrum Jülich GmbH, Corrensstraße 46, 48149 Münster, Germany

Abstract

New anode materials beyond graphite are needed to improve the performance of lithium ion batteries (LIBs). Chemical doping with nitrogen has emerged as a simple strategy for enhancing lithium storage in carbon-based anodes. While specific capacity and rate capability are improved by doping, little is known about other key electrochemical properties relevant to practical applications. This work presents a systematic evaluation of electrochemical characteristics of nitrogen-doped carbons derived from a biomass source and urea powder as anodes in LIB half- and full-cells. Results show that doped carbons suffer from a continuous loss in capacity upon cycling that is more severe for higher nitrogen contents. Nitrogen negatively impacts the voltage and energy efficiencies at low charge/discharge current densities. However, as the charge/discharge rate increases, the voltage and energy efficiencies of the doped carbons outperform the non-doped ones. We provide insights towards a fundamental understanding of the requirements needed for practical applications and reveal drawbacks to be overcome by novel doped carbon-based anode materials in LIB applications. With this work, we also want to encourage other researchers to evaluate electrochemical characteristics besides capacity and cycling stability which are mandatory to assess the practicality of novel materials.

[*] Corresponding author. Email: agomez28@us.es, Tel: +34 9545 56423
[*] Corresponding author. Email: jrr@us.es, Tel: +34 9545 50963

1. Introduction

Lithium ion batteries (LIBs) are an essential technology for certain purposes such as electric automotive applications and renewable energy sources due to their superior gravimetric and volumetric energy and power densities, and low self-discharge when compared to other energy storage technologies [1-5]. However, a major challenge facing current LIBs is that state-of-the-art graphite anodes can no longer satisfy the ever-growing energy demands in terms of energy density and rate capability [1, 6]. Graphite represents so far the material of choice as negative electrode (=anode) for LIBs due to its combination of appropriate features such as low average discharge potential (≈0.2 V *vs*. Li|Li^+), low cost and low voltage hysteresis yielding high energy efficiencies [7-10]. Unfortunately, graphite-based anode materials typically display a poor rate capability, especially at high charging rates ("fast charging") and/or at low operating temperature, which results in a high risk for lithium metal plating at the graphite anode surface [8]. In turn, high charging rates might have a significant impact on the lifetime and safety of LIB cells. Despite intensive efforts to develop alternative anode materials [11], carbon-based electrodes are still at the forefront of research due to their low cost, tunable structure and possible eco-friendly synthesis route by direct carbonization of sustainable biomass resources [12, 13].

In previous works, alternative electrodes based on either nanostructured disordered carbons [14], graphene [15] or heteroatom-doped disordered carbons [16, 17] have shown promising rate capabilities as anode materials for LIBs owing to the shortened diffusion pathways of Li ions and minimized diffusive resistance. Doping of carbon precursors with surface heteroatoms, such as sulfur, boron, phosphorus and nitrogen, is a straightforward strategy to modify the physicochemical and electronic properties of a host carbon network [18]. In the case of LIBs, the addition of surface heteroatoms into carbon scaffolds typically results in additional Li ion adsorption sites and improved electrode wettability in comparison to non-doped carbons [19]. Among the different dopants, nitrogen has drawn the most attention because of the enhanced polarity and electronic conductivity, added active sites within the carbon lattice [20, 21] and stronger electronegativity of nitrogen (χ=3.04) compared to that of carbon atoms (χ= 2.55) according to Pauling scale [22]. Nitrogen atoms incorporated into a carbon network can strengthen the interaction between anchor sites doped with nitrogen and alkali metal ions due to the improved local density [18], which favors the insertion and reduces the charge transfer resistance and diffusion barriers [16]. The process of lithiation (charge) of nitrogen-doped carbons is believed to take place not only through a diffusion process entailing Li

insertion between adjacent graphene layers, but also through a capacitive process, *i.e.*, by surface redox pseudo capacitance and/or double-layer capacitance, attributed to Li adsorption at the surface of nitrogen heteroatoms [23, 24].

Routes previously addressed in literature for doping carbons with nitrogen-heteroatoms can be distinguished as "*in-situ*" and "*post*" treatments [25]. Direct formation treatments include thermal annealing in ammonia flowing atmosphere [26], arc-discharge methods [27], liquid plasma methods [28] and chemical vapor deposition [29]. However, these processes are expensive, afford little control over doping homogeneity and have low yields. Post-treatment methods include hydrothermal treatment [30] and pyrolysis of nitrogen-rich precursors or of carbon resources mixed with nitrogen-rich compounds [31]. One easy, inexpensive and eco-friendly method involves the mixing of carbon materials (or biomass resources [32]) with low-cost nitrogen-rich precursors such as urea and melamine followed by thermal annealing under inert atmosphere [33, 34]. During pyrolysis, the decomposition products of urea or melamine are incorporated into the resulting carbon, doping the surface with nitrogen. This process enables controlling the final nitrogen content by the mass ratio between nitrogen and carbon sources, and peak treatment temperature.

Previous works have reported an increase in reversible capacity and an improvement in rate capability with increasing nitrogen content [17, 30, 35-40] sparking interest in its use as a dopant in silicon anodes [41] and other emerging post-LIB technologies such as sodium ion batteries [42, 43], lithium-sulfur batteries [44], lithium ion capacitors [45] and potassium ion batteries [46, 47]. Most of the works available in the literature only focus on improving reversible capacities and rate capability of these anode materials, disregarding other parameters of crucial importance – *e.g.* Coulombic efficiency (C_{Eff}), average de-lithiation (discharge) potential and voltage (V_{Eff}) and energy (E_{Eff}) efficiencies [10]. In particular, little attention is being paid to the large voltage hysteresis, high working de-lithiation potential and sloping-trend often observed in the potential profile of some nitrogen-doped carbons [48], in contrast to potential plateaus observed for lithiation/de-lithiation of graphite. While it is true that these characteristics could be suitable for supercapacitor applications [49], they also inevitably impact the cell voltage (= difference between positive and negative electrode potential) for LIB applications as a high negative electrode working potential, reduces the cell voltage and, thus, the energy density of a LIB cell. It is not clear to which extent these electrochemical features could limit the application of these materials for LIBs applications, making it necessary to perform a critical evaluation of this point as a function of the nitrogen doping level.

In this work, a comprehensive analysis of electrochemical properties of nitrogen-doped carbons as anode materials for LIB cells was performed. As representative and simple route, nitrogen-doped porous carbons were synthetized by a two-step process. First, a biomass resource as carbon precursor and urea powder as nitrogen precursor were homogenized by a ball-milling process. Afterwards, the mixtures were subsequently pyrolyzed under an inert atmosphere. Different carbon precursors and urea powder weight ratios were considered to study the effect of final nitrogen content on microstructural and textural features. The electrochemical properties of the resulting materials were critically evaluated as LIB anode materials in a half-cell [50] and pseudo full-cell setup with a capacity-overbalanced lithium nickel cobalt manganese oxide (NCM-111) cathode. Special attention was paid to the correlation between the N-doped carbon material properties and electrochemical characteristics, including the reversible capacity, rate capability, C_{Eff} as well as V_{Eff} and E_{Eff}. Post-mortem X-ray photoelectron spectroscopy (XPS) was used for investigating the surface chemistry of cycled electrodes.

2. Methods

2.1. Materials

As-received olive stones (supplied by *OleoMorón S.L*) were first ground and sieved to a particle size lower than 75 µm. As a route to introduce homogeneous nitrogen-based surface functionality into the carbon material, olive stone powder was then mixed with urea powder ($CO(NH_2)_2$, purity ≥ 98%, *Sigma Aldrich*) by a planetary ball-mill (Pulverisette 6, *Fritsch*). The milling process was performed using an agate crucible and grinding agate balls (the ball-to-powder ratio was 3:1; four 13 mm and six 8.3 mm in diameter balls) at a rotation speed of 350 rpm for 2 h. Three different olive stone to urea weight ratios were considered in this study 1:0, 1:1 and 1:5. The resulting mixture was dried at 100 ºC for 48 h and then heated in a tube furnace under a flowing inert atmosphere of nitrogen (flow rate of ≈ 0.2 $L \cdot min^{-1}$, *Alphagaz*, 99.999 %) up to 800 ºC at a heating rate of 5 $ºC \cdot min^{-1}$, followed by a holding time of 60 min and then cooled down to room temperature. To avoid relevant microstructural changes in carbon microstructure and to facilitate investigating the direct influence of the amount of nitrogen dopant, only one peak heat-treatment temperature was considered for all samples.

Resulting carbon materials will be referred throughout the text according to the corresponding weight ratio to as biomass:urea 1:0, 1:1 and 1:5.

2.2. Microstructural and surface characterization

Scanning electron microscopy (SEM, TENEO, *FEI*) and transmission electron microscopy (TEM, *Talos F200S*, *FEI*) analyses were performed to characterize the surface morphology and microstructural features.

Thermal analysis during heat-treatment was studied by thermogravimetric (TGA) and differential scanning calorimetry (DSC) experiments using a dual thermobalance (Thermal Advantage SDT-Q600, *TA Instruments*). Measurements were carried out applying a heating rate of 10 ºC·min^{-1} up to 800 ºC under a nitrogen flow rate of 100 ml·min^{-1}. Calibration tests were periodically performed using a standard sapphire sample.

Raman spectroscopy measurements (Bruker SENTERRA, *Bruker Optics Inc.*) were carried out using a green excitation wavelength of 532 nm and a laser power of 10 mW. In order to collect the spectra, 10 integrations were carried out with a time of 60 s. The spectra shown is the average of three measurements at different sample positions. Raman spectra were fitted to pseudo-Voigt functions using a least-square house-made code implemented in MATLAB considering all the relevant Raman bands of carbon materials.

X-ray photoelectron spectroscopy (XPS) analyses of doped carbon powders were carried out on an *Axis Ultra DLD* spectrometer (*Kratos*) using a monochromatic Al K_α radiation ($h\nu$ = 1486.6 eV; 10 mA emission current and 12 kV accelerating voltage) to analyze the surface composition of carbon materials. The binding energy (BE) was calibrated against the C_{1s} peak of carbon (284.5 eV). To ensure the reproducibility of the results, three measurements per sample were performed. Data processing, curve fitting and peak deconvolution was performed using *CasaXPS* software and pseudo-Voigt line shapes. Atomic concentrations were calculated using integrated peak intensities. Additionally, *post-mortem* XPS investigations of the cycled electrodes (after 100 cycles; biomass:urea 1:0 and 1:5 samples) were performed in order to investigate changes in solid electrolyte interphase (SEI) formation and active lithium losses. For that, electrodes were harvested from cycled pseudo full-cells in an argon-filled glovebox and washed with 200 µL of dimethyl carbonate (DMC; BASF, battery grade) prior to surface analysis, in order to remove electrolyte residues and $LiPF_6$ salt.

Textural properties were evaluated by nitrogen adsorption/desorption measurements at 77 K (ASAP 2420, *Micromeritics*). Prior to the measurement, samples were degassed at 200 ºC overnight under reduced pressure. Specific surface areas were determined by applying the Brunauer-Emmett-Teller (BET) theory to the adsorption isotherms. Pore size distributions were estimated by density functional (DFT) theory.

2.3. Electrode preparation

Carbon samples obtained after heating at 800 °C were first ground with a mortar and pestle and sieved down to 45 µm. Working electrodes (WE) consisted of a mixture of 90 wt. % carbon as the active material, 5 wt. % sodium-carboxymethyl cellulose as the binder (Na-CMC, Walocel CRT 2000 PPA 12, *Dow Wolff Cellulosics*) and 5 wt. % Super C65 as conductive agent (*Imerys Graphite & Carbon).* The WE paste was prepared using deionized waster as solvent. The electrode paste was then completely homogenized by a high-energy T25 *Ultra Turrax* disperser (1 hour, 10.000 rpm) and coated on a dendritic copper foil (*Carl Schlenk AG*) using a doctor blade. Electrode sheets were punched into circular discs (12 mm in diameter (Ø)) and dried under reduced pressure (pressure level below 10^{-2} bar) using a *BÜCHI*® oven at 120 ºC overnight. The average active mass loading of the WE was about 2 - 2.5 $mg \cdot cm^{-2}$.

2.4. Cell assembly and electrochemical characterization

Electrochemical investigations were first carried out in a half-cell configuration using three-electrode Swagelok-type T-cells and high-purity metallic lithium foil (*Albemarle Corporation*, battery grade) as counter (CE) and reference (RE) electrodes. Cells were assembled in a dry room with a dew point of at least -50 °C. 1 M lithium hexafluorophosphate ($LiPF_6$) in ethylene carbonate (EC)/ethyl methyl carbonate (EMC) 3:7 (w:w) plus 2 wt. % vinylene carbonate (VC) as SEI forming additive [51] was used as the electrolyte (supplied by *BASF SE*). Six and three-layers *Freudenberg* FS2190 discs (Ø = 13 mm in diameter between WE and CE and Ø = 8 mm in diameter for RE) were used as separators. The separators for the WE/CE and RE were wetted with 120 µL and 80 µL of electrolyte, respectively.

For the electrochemical investigations in carbon || Li metal cells, constant current charge/discharge experiments were carried out within cut-off potentials between 0.02 (lithiation) and 1.5 V (de-lithiation) *vs.* $Li|Li^+$ using a *Maccor Series 4000* automated test system (*Maccor, Inc.*). For comparison, electrochemical properties of a commercial synthetic graphite as anode material for LIBs (SMG A4; active mass loading 2.3 $mg \cdot cm^{-2}$, BET specific surface area 1.58 $m^2 \cdot g^{-1}$, average particle = 4.32 ± 0.04 µm, *Hitachi*) were also investigated. Rate experiments at different specific currents between 37.2 $mA \cdot g^{-1}$ to 7440 $mA \cdot g^{-1}$ were carried out as follows: first three formation cycles at 37.2 $mA \cdot g^{-1}$, followed by 5 cycles at 372 $mA \cdot g^{-1}$ and each 5 cycles at specific currents of 37.2, 74.4, 186, 372, 744, 1166, 1860, 3720, and finally, 10 cycles turning back to 372 $mA \cdot g^{-1}$. Biomass:urea 1:0 and 1:5 samples were also studied at specific currents of up to 7440 $mA \cdot g^{-1}$. Long-term cycling stability experiments (carbon || Li metal cells) were carried out by performing three formation cycles at 37.2 $mA \cdot g^{-1}$ and then 200 cycles at 186 $mA \cdot g^{-1}$ in a potential window between 0.02-1.5 V *vs.* $Li|Li^{+\cdot}$

In order to evaluate reaction mechanisms, cyclic voltammetry (CV) experiments were carried out in a potential range between 0.02 and 1.5 V *vs.* $Li|Li^+$ by using a VMP multichannel potentiostatic–galvanostatic system (*Biologic Science Instruments*) connected to a climatic chamber at 20 °C (KBF 115, *Binder*). For estimation of capacitive reaction and diffusion reaction contributions, CV experiments were performed at different scan rates: first three SEI formation cycles at 0.1 $mV \cdot s^{-1}$, followed by 3 cycles at 0.2, 0.4, 0.6, 0.8, 1, 2, 5, 10 and 20 $mV \cdot s^{-1}$.

Further electrochemical investigations were performed in a LIB pseudo full-cell setup. Three-electrode Swagelok-type T-cells consisting of Li metal as RE, nitrogen-doped biomass derived carbon as negative electrode and a capacity-oversized lithium nickel cobalt manganese oxide ($LiNi_{1/3}Mn_{1/3}Co_{1/3}O_2$, NCM-111) as positive electrode was considered in order ensure excess of active lithium within the cell. The capacity-oversized NCM-111 electrodes were produced by an in-house pilot line (95 wt.% active material, 3wt. % PVDF as binder and 2 wt.% Super C65 as conductive agent) with an areal capacity of ≈2.3 $mAh \cdot cm^{-2}$, resulting in an anode to cathode capacity balancing of ≈1:2.3 in the pseudo full-cell investigations. Three-layer *Freudenberg* FS2190 discs (Ø = 13 mm in diameter between WE and CE and Ø = 8 mm in diameter for RE) were used as separators. Long-term cycling stability experiments (NMC-111 || carbon full-cells) were carried out by performing three formation cycles at 37.2 $mA \cdot g^{-1}$ and then 100 cycles at 186 $mA \cdot g^{-1}$. During these pseudo full-cell experiments, the cut-off potentials of the negative electrodes were controlled and set to 0.02 V *vs.* $Li|Li^+$ and 1.5 V anode *vs.* $Li|Li^+$. For all experimental cycling experiments, three cells were evaluated for each sample to ensure a high reproducibility of the results. The associated standard deviation is represented as error bars in the corresponding figures.

The C_{Eff}, (in %) of a lithium ion cell is an indicator of the reversibility of redox reactions and reflects the ratio of the delivered discharge capacity (=de-lithiation in this case) (Q_d) to the capacity necessary to charge (=lithiation in this case) (Q_c) the system over a full cycle [52]. This parameter should be close to 100 % and it is generally expressed in percentage as follows [53]:

$$C_{Eff}\,(\%) = 100 \cdot \frac{Q_d}{Q_c} \qquad (1)$$

The E_{Eff} and V_{Eff} reflect the ratio of the discharge energy/voltage to the charge energy/voltage, respectively [54]. When a constant current is applied in charge/discharge cycling experiments, E_{Eff} and V_{Eff} can be defined as follows:

$$E_{Eff}\,(\%) = 100 \cdot \frac{\int_0^{t_d} U_d I_d dt}{\int_0^{t_c} U_c I_c dt} \qquad (2)$$

$$V_{Eff}\ (\%) = 100 \cdot \frac{\overline{U_d}}{\overline{U_c}} \quad (3)$$

Where U_d and U_c represent the discharge and charge cell voltages, I_d and I_c the discharge and charge current and t_d and t_c represent the discharge and charge time, respectively. $\overline{U_d}$ and $\overline{U_c}$ refer to the average discharge voltage and average charge voltage, respectively. When a constant current is applied, the E_{Eff} can be defined as the product of C_{Eff} and V_{Eff} as follows:

$$E_{Eff} = C_{Eff} \cdot \frac{\frac{\int_0^{t_d} U_d dt}{t_d}}{\frac{\int_0^{t_c} U_c I_c dt}{t_c}} = C_{Eff} \cdot \frac{\overline{U_d}}{\overline{U_c}} = C_{Eff} \cdot V_{Eff} \quad (4)$$

The V_{Eff} and E_{Eff} were estimated following the work of *Meister et al*. [10]. For the calculations, a virtual lithium iron phosphate (LFP) cathode with a constant potential of 3.4 V *vs.* $Li|Li^+$ was considered as the positive electrode. The average de-lithiation working potential was defined at half of the discharge/de-lithiation capacity.

3. Results and discussion

3.1. Material characterization

Nitrogen-doped carbons were synthetized by a pyrolysis process of a mixture of olive stones as carbon source and urea powder as nitrogen-rich source. The thermal behavior during pyrolysis was investigated by TGA/DSC analysis, and results are detailed in **Figure S1** (Supplementary Information). The remaining yield decreased from 30 wt. % to 5 wt. % when increasing the biomass:urea weight ratio from 1:0 to 1:5.

Figure 1-a, b shows scanning electron microscope (SEM) micrographs of representative samples. The carbon scaffold derived from the raw biomass precursor (**Figure 1-a**; biomass:urea 1:0) exhibits a porous structure with micron-sized slits and non-directional cylindrical pores. After the ball-milling homogenisation process with urea powder and subsequent pyrolysis process (**Figure 1-b**; biomass:urea 1:5), the resulting carbon preform shows a more irregular surface morphology with no evident porous channels. Close-up high-resolution TEM images (**Figure 1-c**) of doped carbon (biomass:urea 1:5 sample) shows a typical turbostratic disordered microstructure composed by a network of nanosized carbon crystallites arranged in randomly-oriented layers, according to the non-graphitizable nature of biomass [55]. No evident difference in such a microstructure was observed while varying the urea content ratio. The EDX elemental mappings of biomass:urea 1:5 sample shown in Figure **1-d-g** prove the uniform distribution of nitrogen (green coloured area, **Figure 1-f**) on the carbon particle surface (red coloured area, **Figure 1-e**). The remaining oxygen present in the sample

(blue coloured area, **Figure 1-g**) comes from the uncompleted thermal decomposition of polysaccharide chains of lignocellulosic-based polymers at a pyrolysis temperature as low as 800 ºC.

The surface chemical composition and nitrogen bonding configuration of doped carbons was further analysed by XPS. A summary of integrated atomic concentrations is listed in **Table 1**. The full-range XPS survey spectra (shown in the Supplementary Information, **Figure S2**) exhibits characteristic peaks centred at ≈285, 400, 533 eV, corresponding to C_{1s}, N_{1s} and O_{1s}, respectively. Impurity phases of Si (< 4 at. %) and Na (< 2 at. %) were also detected, which may be inherent to the olive stone precursor and can be attributed to the inorganic fraction often incorporated during biomass growth [56]. The carbon content was ≈80 at. % irrespectively of the sample. With an increase in the starting urea content, nitrogen atomic concentration ranged between 0, 4.1 and 12.7 at. % for biomass:urea 1:0, 1:1 and 1:5 samples, respectively (**Table 1**). Thus, these results in combination with TEM elemental mapping confirm that the mixing of the biomass precursor with urea powder helped in homogeneously doping the resulting carbon scaffold with nitrogen. In contrast, the oxygen content decreased from 13 to 3 at. % from the sample with the highest concentration (biomass:urea 1:5) to that with the lowest concentration (biomass:urea 1:0) of nitrogen species.

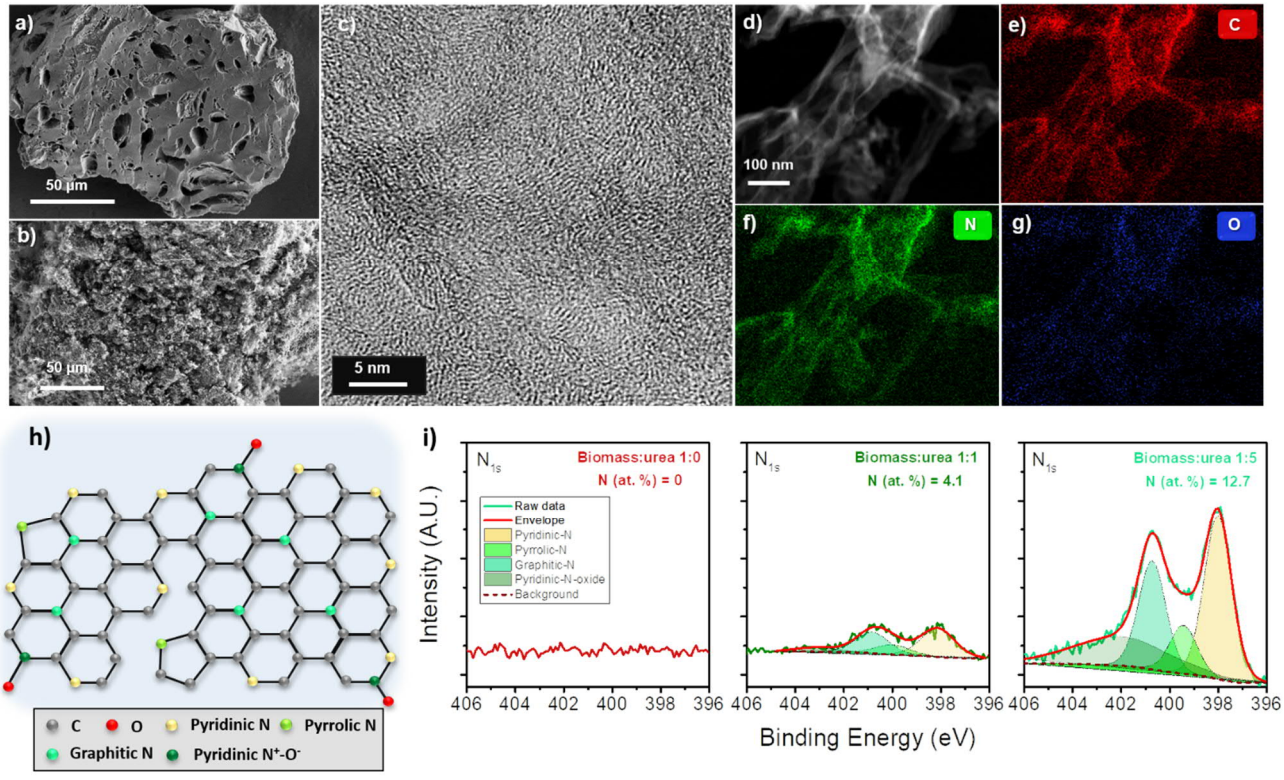

Figure 1. Representative SEM micrographs of a) biomass:urea 1:0 and b) biomass:urea 1:5 samples. c) Representative TEM micrograph of biomass:urea 1:5 sample. EDX elemental mappings of biomass:urea 1:5 sample (d) corresponding to e) C, f) N and g) O. h) Schematic structure of nitrogen-doped graphene monolayer. i) Results of N_{1s} spectra fitting of XPS analysis.

The typical microstructure of nitrogen-doped graphene planar sheets is proposed to be similar to that shown in **Figure 1-h** [57]. In other to shed light on the bonding state of the nitrogen surface groups, **Figure 1-i** shows the high resolution N_{1s} core level XPS spectra along with the fitting of nitrogen chemical states for all biomass-derived carbon samples. Generally, the N_{1s} region can be deconvoluted into four nitrogen bonding configurations using Gaussian-Lorentzian functions: pyridinic nitrogen (≈398.7 eV) [58], pyrrolic nitrogen (≈400.3 eV), graphitic or quaternary nitrogen (≈401.4 eV) and pyridinic oxidized nitrogen (≈402-405 eV) [59, 60]. Pyridinic atoms are located at the edge sites of graphene layers, substituting one atom within hexagonal carbon rings and contributing one pair of lone electrons to the π-system. Pyrrolic nitrogen disrupts the planar structure of graphene and it is bonded between two carbon atoms on a five-membered ring, contributing two pairs of lone electrons to the π-system. It is well-known that both pyridinic and pyrrolic nitrogen create additional defects and a greater disorder within the graphene lattice [47, 61]. Graphitic nitrogen is located inside the graphitic carbon plane bonded with three sp^2 carbon atoms [62], increasing the electron density within the delocalized π-system [37, 63].

The composition of each nitrogen bonding configuration considering the total nitrogen content in each sample is summarized in **Table 1**. The relative nitrogen composition for the biomass:urea 1:5 sample was estimated to be 39 % pyridinic-N, 11 % pyrrolic-N, 26 % graphitic-N and 24 % pyridinic-oxidized N. Pyridinic, pyrrolic and graphitic nitrogen absolute contents increased likewise up to 2.5 times when increasing the starting urea amount from 1:1 to 1:5. According with XPS analysis, carbons were thus dominantly doped with pyridinic and graphitic nitrogen bonding configurations as a result of the decomposition of the urea precursor during thermal treatment.

The structural order of nitrogen-doped carbons was characterized by Raman spectroscopy measurements. Detailed discussion can be found in the Supplementary Information (**Figure S3** and **Table S1**). The increase in the starting urea concentration and thus the nitrogen content results in an increase in the full widths at half-maxima (FWHM) for the D_1-mode, an increase of the D_1/G ratios and a downshift of the G band from 1580 to 1563 cm^{-1}, meaning an increase of defect sites within the graphene lattice by surface doping. Since textural properties are known to have a great impact on the formation of the SEI on the carbon anode surface in the first charge/discharge cycle(s) [64], [65], a detailed discussion of adsorption/desorption isotherm and pore size distribution can be found in the Supplementary Information (**Figure S4**). The BET specific surface areas were ≈189.5, 212.5 and 140.4 $m^2 \cdot g^{-1}$ for biomass:urea 1:0, 1:1 and 1:5 samples, respectively.

3.2. Electrochemical characterization

3.2.1. Electrochemical investigations in carbon || Li metal cells

For getting further insights into the influence of the nitrogen-doping level on the electrochemical properties, synthetized carbons were first investigated as anode materials in a half-cell configuration (carbon (WE) || Li metal (CE)) with a special focus on rate capabilities and maximum specific capacities. Electrochemical properties of a commercial graphite anode are also included for comparison purposes.

Figure 2-a shows the rate performance of different anode materials at specific currents ranging from 37.2 $mA \cdot g^{-1}$ to 7440 $mA \cdot g^{-1}$, whereas **Figure 2-b** compares the capacity retention (considering the maximum capacity (100 %) as the one achieved at a specific current of 37.2 $mA \cdot g^{-1}$) as a function of specific current to better evaluate the rate capability. Maximum average specific capacities of 274 $mAh \cdot g^{-1}$ (biomass:urea 1:0), 349 $mAh \cdot g^{-1}$ (biomass:urea 1:1), 352 $mAh \cdot g^{-1}$ (biomass:urea 1:5) and 338 $mAh \cdot g^{-1}$ (graphite) were achieved at the lowest specific current of 37.2 $mA \cdot g^{-1}$. As can be seen, N-doped carbons exhibit de-lithiation capacities in the range of commercial graphite anodes (which typically show a practical capacity of up to 360 $mAh \cdot g^{-1}$), which may be related to the large proportion of nitrogen species or the existence of a more disordered carbon structure [66, 67]. Up to a specific current of 186 $mA \cdot g^{-1}$, there is no obvious difference in the behaviour of 1:1 and 1:5 samples in terms of the maximum specific capacity. Nevertheless, biomass:urea 1:5 exhibits a less-pronounced capacity drop at increased rates compared to the pure carbon sample (biomass:urea 1:0), suggesting the importance of the nitrogen content on rate capability. There is previous evidence that pyridinic nitrogen is responsible for attaining higher reversible capacities of nitrogen-doped anodes in LIB cells [62, 68]. *Cao et al.*[20] theoretically proved that pyridinic and pyrrolic nitrogen would promote the diffusion of lithium ions due to the high energy binding at edges and defect sites within the carbon structure [69]. In contrast, graphitic nitrogen is believed to improve the charge/discharge performance, but does not enhance the penetration of lithium ions trough the basal plane of the carbon structure [69]. At 744 $mA \cdot g^{-1}$, the specific capacities drop to 129 $mAh \cdot g^{-1}$ (biomass:urea 1:0), 168 $mAh \cdot g^{-1}$ (biomass:urea 1:1), 207 $mAh \cdot g^{-1}$ (biomass:urea 1:5) and 140 $mAh \cdot g^{-1}$ (graphite) corresponding to 47, 48, 58 and 41% retention of the maximum achievable capacity, respectively. Interestingly, at a high specific current of 3720 $mA \cdot g^{-1}$, the reversible capacity of biomass:urea 1:5 sample still remains ≈116 $mAh \cdot g^{-1}$, meaning a retention of ≈32 % of their maximum capacity. This value considerably outperforms the rate capability of commercial graphite and the undoped carbon sample, which retain only 4 and 8 % of their maximum capacity at this point, respectively. For nitrogen-doped carbons, the rate capability is thus improved as the doping level is further increased. When the specific current is restored back to 372 mA g^{-1}, slightly

lower capacities compared to those at the beginning of the C-rate experiments were recovered, suggesting limited cycling stability.

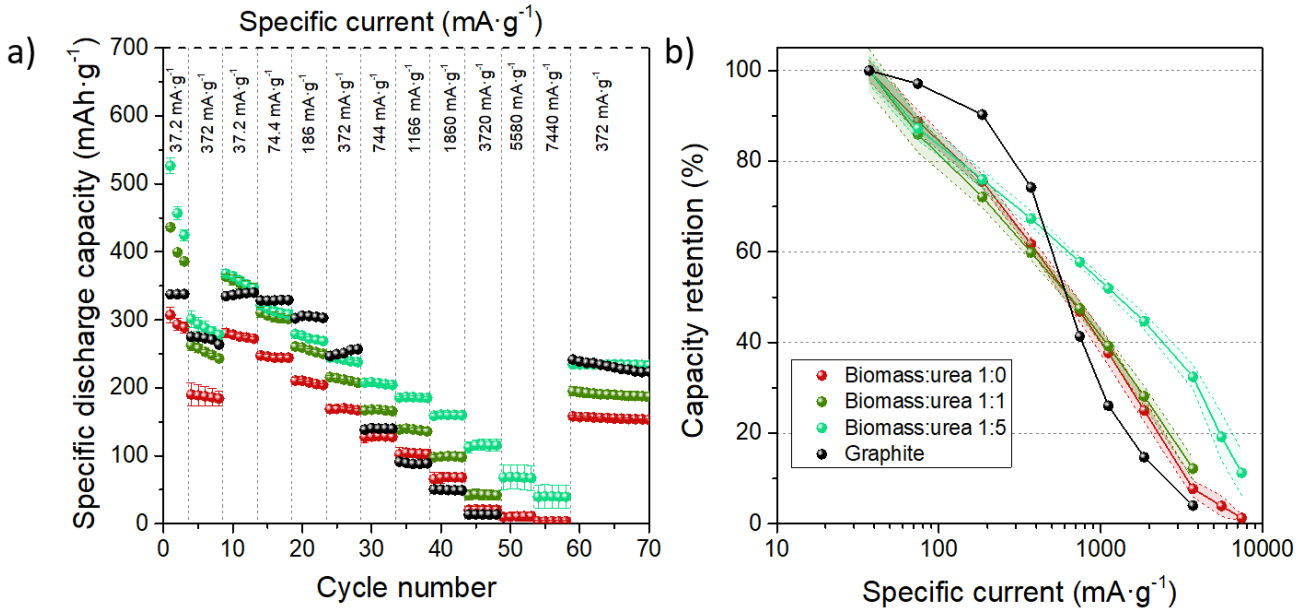

Figure 2. Rate capability of different anode materials: a) Specific discharge capacity *vs.* cycle number using specific charge/discharge currents between 37.2 and 7440 $mA \cdot g^{-1}$ and b) Capacity retention as a function of specific charge/discharge current, whereas the capacity at 37.2 $mA \cdot g^{-1}$ was defined as 100 % for each material. Error bars: standard deviation of three cells for each sample. Rate performance investigations: Cycles 1 - 3: 37.2 $mA \cdot g^{-1}$; Cycles 4 - 8: 372 $mA \cdot g^{-1}$; Cycles 9-59: specific currents of 37.2, 74.4, 186, 372, 744, 1166, 1860, 3720, 5580 and 7440 $mA \cdot g^{-1}$ for each step 5 cycles; Cycle 60 - onwards: 372 $mA \cdot g^{-1}$. Half-cell setup: carbon (WE)||Li metal (CE) cells using Li metal as RE. Potential range: 0.02 -1.5 V *vs.* $Li|Li^+$.

Detailed discussion about long-term investigations in carbon || Li metal cells are included in the Supplementary data (**Figure S5** and **S6**). At first glance, it seems clear from the results presented so far that a greater doping level will result in a better rate capability and higher maximum reversible capacity. Despite this, these materials also have limitations that are not directly visible by the C-rate cycling experiments. The irreversible capacity however steadily increases with a higher presence of nitrogen doping, although the long-term stability will also be studied in the next section using more practical conditions on LIB full-cells.

The evolution of C_{Eff}, V_{Eff} and E_{Eff} as a function of the specific current is summarized in **Figure 3-a-c**. Values represent an average of four cycles after the specific current change in the C-rate experiment (see *Methods* for further details). Apart from having a significant impact on the specific capacity, the increase in current and the starting nitrogen content has also an effect on the E_{Eff}. At 37.2 $mA \cdot g^{-1}$, E_{Eff} average values of ≈91% (biomass:urea 1:0), ≈87% (biomass:urea 1:1), ≈86% (biomass:urea 1:5) and ≈97% (graphite) were reported. Hence, the reachable E_{Eff} becomes smaller with increasing nitrogen content at the lowest specific current. As the E_{Eff} is the ratio of the discharge energy to the charge

energy, values below 100% indicate that the useful output energy is lower than the input energy. Furthermore, as the E_{Eff} is the product of C_{Eff} and V_{Eff}, changes are directly related to either parasitic reactions, having an impact on the C_{Eff}, or by the voltage hysteresis during charge/discharge influencing the V_{Eff}. In general, the voltage hysteresis for battery materials increases with increasing specific current, resulting in a lower V_{Eff} and therefore decreased E_{Eff} [10]. Such a trend is however counteracted for the nitrogen-doped materials in the specific current range from 186 $mA \cdot g^{-1}$ to 744 $mA \cdot g^{-1}$. While the undoped carbon and graphite electrodes follow a monotonically declining trend upon increasing the specific current, the E_{Eff} increases for biomass:urea 1:5 (left grey dashed area). As can be seen in **Figure 3-a**, the E_{ff} of biomass:urea 1:5 sample remains almost constant up to 1860 $mA \cdot g^{-1}$ (red area) and then abruptly decreases when the rate is further increased (right grey area). At 3720 $mA \cdot g^{-1}$, E_{Eff} values drop to ≈72 % (biomass:urea 1:0), ≈73 % (biomass:urea 1:1), ≈81 % (biomass:urea 1:5), ≈81 % (graphite).

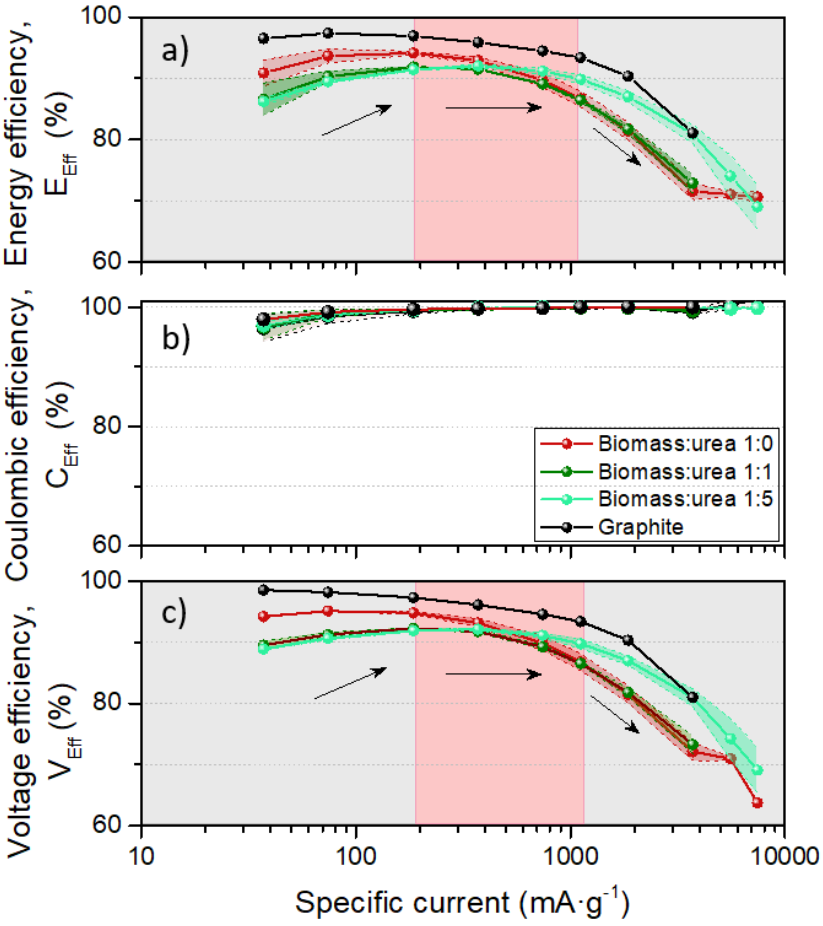

Figure 3. Evolution of a) E_{Eff}, b) C_{Eff} and c) V_{Eff} at different charge/discharge currents. Potential range: 0.02 V - 1.5 V *vs.* $Li|Li^+$. Half-cell setup: carbon (WE)||Li metal (CE) cells using Li metal as RE. Error bars: standard deviation of three cells for each sample. The red dashed area points out the range where nitrogen-doped samples maintain constant E_{Eff} and V_{Eff} despite the increase in specific current. The black arrows indicate the evolution of the trend for the biomass:urea 1:5 sample.

As shown in **Figure 3-b**, the C_{Eff} (after three formation cycles) is above 96% for all samples independently of the applied charge/discharge current. Interestingly, the lowest C_{Eff} of ≈96% is achieved for the biomass:urea 1:5 sample at a specific current of 37.2 $mA \cdot g^{-1}$, which then progressively rises to ≈99% at higher currents.

As the E_{Eff} is the product of C_{Eff} and V_{Eff} and the contribution from the C_{Eff} is small, the E_{Eff} trend in our samples is in turn more influenced by the V_{Eff}. It can be confirmed from **Figure 3-c** that the V_{Eff} follows a similar trend than the one shown by the E_{Eff}. While the V_{Eff} progressively decreases for biomass:urea 1:0, biomass:urea 1:1 and graphite samples, it increases up to 372 $mA \cdot g^{-1}$ (left grey dashed area), remains almost constant up to 1860 $mA \cdot g^{-1}$ (red dashed area) and then decays when increasing the rate (right grey dashed area) for biomass:urea 1:5 sample with the highest concentration of nitrogen (12.7 at. %). Among the investigated carbons from biomass resources, non-doped carbon (biomass:urea 1:0) shows the highest V_{Eff} and E_{Eff} at low currents, whereas the most doped carbon (biomass:urea 1:5) exhibit a better performance at high currents.

V_{Eff} and thus E_{Eff} values are directly related to the development of the voltage hysteresis between the lithiation (charge) and de-lithiation (discharge) potential profiles. **Figure 4-a-c** shows the potential profiles of investigated anode materials at different specific currents as a function of the normalized capacity (37.2 $mA \cdot g^{-1}$ (**a**), 372 $mA \cdot g^{-1}$ (**b**) and 1116 $mA \cdot g^{-1}$ (**c**)). For ease of comparison of the influence of rate increase on the potential profile for different anode materials, see **Figure S7** (Supplementary Information). **Table S2** shows a quantification of the voltage hysteresis at a fixed normalized capacity of 0.5. The potential and V_{Eff} trends differ considerably depending on the type of anode material. The potential profile of the graphite anode at low currents exhibits different plateaus, indicating the transition between different staging phases at potentials below ≈0.2 V *vs.* $Li|Li^+$, and a small hysteresis. The charge/discharge potential profile of biomass-derived carbon differs considerably from that of graphite, as the reversible insertion of Li^+ begins at potential above 1.0 V (*vs.* $Li|Li^+$) and slopes without discernible plateaus as a consequence of the disordered structure and non-equivalent insertion sites. The almost linear charge/discharge potential profile of highly doped carbons suggest a dominant capacitive storage mechanism. During the lithiation process, parts of the Li ions are inserted within parallel graphene sheets, contributing to diffusive storage, whereas the rest of Li ions are adsorbed at the surface of carbon atoms or bound to nitrogen atoms, contributing to capacitive storage [24]. Kinetic analysis performed by *Zheng et al.*[23] suggested that the capacitive-charge-storage contributions increase with increasing the rate owing to the adsorbed Li onto the carbon surface, hence, resulting in a superior rate capability compared to graphite anodes. These findings are in agreement with those reported by *Tian et al.*[24], which suggested that the Li insertion within

graphene layers is limited at high rates, being the high-capacity a result of dominant Li^+ reactions with pyridinic nitrogen. To study electrochemical reaction kinetics and make an estimation of the capacitive and diffusion-dominant mechanism contributions, we performed additional CV measurements at different sweep rates from 0.1 to 20 $mV \cdot s^{-1}$. CV results of different carbon anodes are shown in **Figure S8** (Supplementary data). Surface-induced and diffusion-controlled mechanism contributions to total Li storage can be estimated using a power law of the form $i = av^b$, where *i* and *v* represents the current and the sweep rate, respectively [70]. The value of *b* can be determined by the linear slope of the log i vs. log v plot. Typically, *b*=0.5 indicates a diffusion-controlled response (Li insertion/extraction), while *b*=1.0 represents a capacitive response (double-layer surface-induced pseudo/capacitance). A *b* value from 0.5 to 1.0 indicates a "*transition*" area between pseudocapacitive materials and battery-type materials, although a clear boundary is not easy to define. Due to the absence of clear peak current in the CV curves (especially in the biomass:urea 1:5 sample) we considered the potentials at which the current intensity peaks as both anodic and cathodic peaks. As can be seen in **Figure S8-d-f**, the *b*-value is close to 0.5 in all cases for the anodic process, but progressively increases up to 0.77 for the cathodic peak. According to our results, the storage process is thus a combination of capacitive effect, associated with Li^+ adsorption on the carbon surface, and a diffusion-limited process.

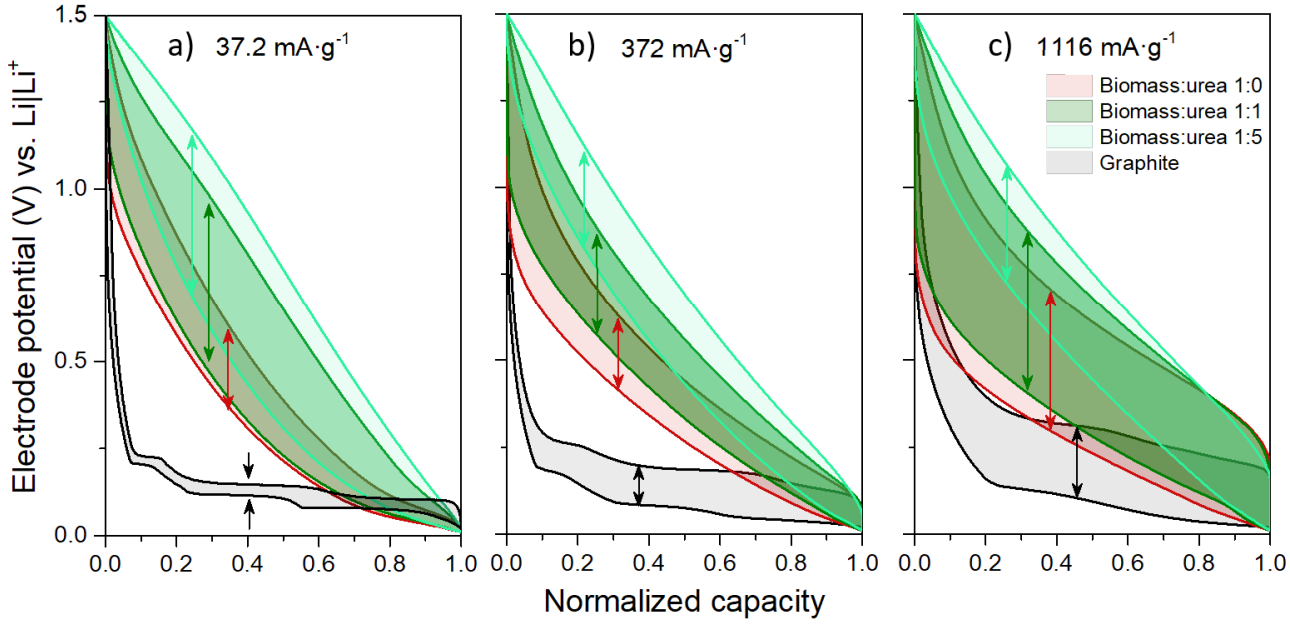

Figure 4. Representative potential as a function of the normalized capacity at a) 37.2 $mA \cdot g^{-1}$, b) 372 $mA \cdot g^{-1}$ and c) 1116 $mA \cdot g^{-1}$. The shadowed areas and arrows highlight the hysteresis between charge/discharge processes. Half-cell setup: carbon (WE)||Li metal (CE) cells using Li metal as RE.

The redox activity at the surface of nitrogen-doped carbon crystallites may also be the responsible for the extended capacity contribution at potentials above 1 (*vs.* $Li|Li^+$). At 37.2 $mA \cdot g^{-1}$, the voltage hysteresis of biomass-derived carbons (see **Table S2** for better quantification) seems to increase

proportionally to the content of nitrogen-functional groups and considerably exceeds to that of graphite, meaning that the Li insertion occurs at a more negative potential than the Li de-insertion. Although not investigated in detail for nitrogen-doped carbons, the voltage hysteresis in hydrogen-containing carbons is believed to be caused by the difference in energy involved in the change of the bonding of the nearby carbon atoms [71]. While the V_{Eff} is higher at low currents, this tendency is reversed at higher currents. In turn, at 1116 $mA \cdot g^{-1}$, the lower voltage hysteresis (**Table S2**) of biomass:urea 1:5 sample as compared to less doped carbons results in a higher V_{Eff} (and thus a higher E_{Eff}).

At 37.2 $mA \cdot g^{-1}$, average de-lithiation potentials were ≈0.49 V (biomass:urea 1:0), ≈0.67 V (biomass:urea 1:1), ≈0.77 V (biomass:urea 1:5) and ≈0.18 V (graphite) *vs.* $Li|Li^+$. The average de-lithiation potential is a key parameter for application as anode materials in LIB cells and it should be as low as possible to increase the cell voltage and thus to achieve the maximum energy density, while still being sufficiently high to avoid Li metal plating at the top of the anode, *e.g.*, during fast-charging. The low working potential and almost constant potential profile (≈0.2 V vs. $Li|Li^+$) of graphite makes it an ideal anode material for LIB cells. A raised average de-lithiation potential as a result of a large hysteresis negatively affects the cell voltage in a full-cell setup. The application of nitrogen-doped carbons for applications requiring high-energy density would be thus strongly hindered compared to graphite, as they turn out to be more suitable for high-power applications.

As for conversion-type electrode materials, nitrogen-doped carbons can also enhance the reversible capacity at the expense of increasing the cut-off potential above 1.5 V vs $Li|Li^+$. **Figure 5-a** displays the influence of increasing the cut-off potential from 1.5 to 3 V (*vs.* $Li|Li^+$) at 186 $mA \cdot g^{-1}$, whereas **Figure 5-b** shows corresponding representative potential profiles of biomass:urea 1:5. While in less-doped samples (biomass:urea 1:0 and biomass:urea 1:1) this change does not impact as much, the specific capacity for the biomass:urea 1:5 electrode can increase from ≈300 $mAh \cdot g^{-1}$ (0.02-1.5 V *vs.* $Li|Li^+$) to ≈380 $mAh \cdot g^{-1}$ (0.02-3.0 V *vs.* $Li|Li^+$) by increasing the cut-off potential due to an enhanced sloping contribution above 1.5 V (*vs.* $Li|Li^+$). All the nitrogen content may not be contributing to storage process when setting an upper cut-off potential of 1.5 V (*vs.* $Li|Li^+$). It is generally believed that the capacity below 0.5 V (*vs.* $Li|Li^+$) is related to Li insertion into graphene layers, whereas the capacity above 0.5 (*vs.* $Li|Li^+$) is related to surface-dominated reactions resulting from the adsorption of Li^+ on pyridinic or pyrrolic defect structures [24, 72]. The work of *Hu et al.* [73] suggested that the pyridinic nitrogen dominated the capacity enhancement at a potential below 3 V (*vs.* $Li|Li^+$), while the pyrrolic nitrogen contributed to the Li-ion storage below 1.5 V (*vs.* $Li|Li^+$). However, although

commonly disregarded in the majority of works on doped carbons, it has to be noted that an enhanced upper cut-off potential could stress the electrode, speeding up ageing effects or resulting in the oxidation/dissolution of the SEI layer or even of the Cu current collector (above ≈3.5 V *vs.* Li|Li$^+$)[74].

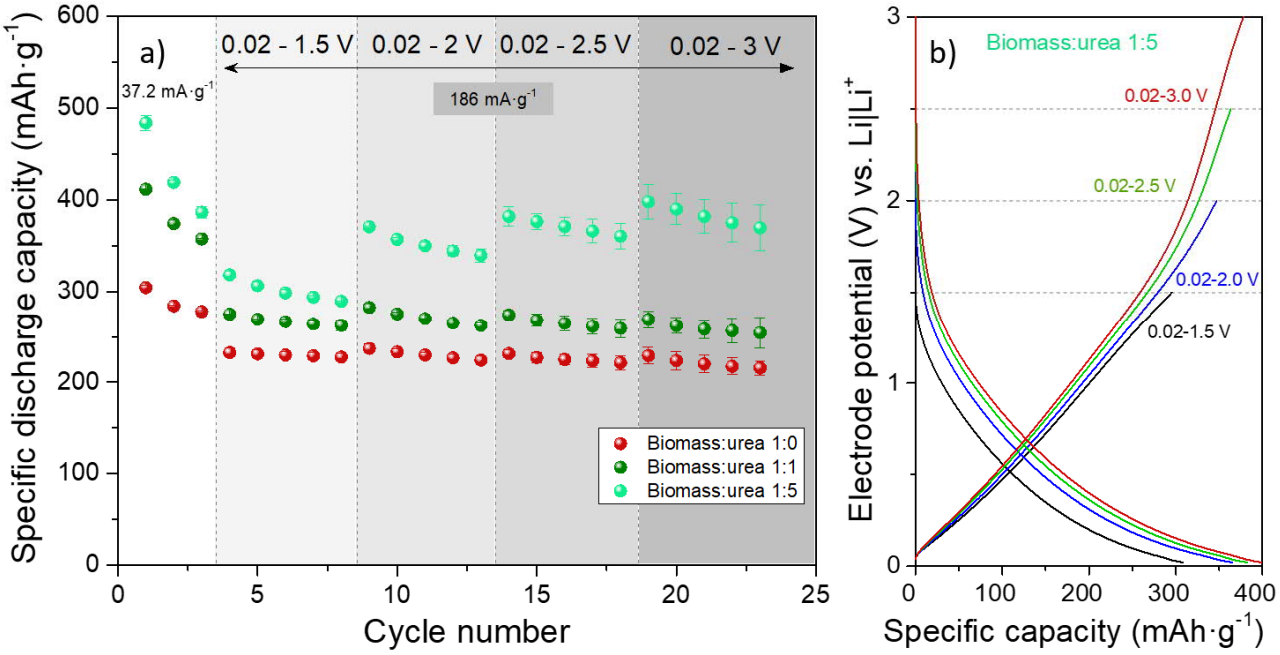

Figure 5. a) Specific discharge capacities and b) representative potential profiles at different upper cut-off potentials from 1.5 to 3.0 V *vs.* Li|Li$^+$. Half-cell setup: carbon (WE)||Li metal (CE) cells using Li metal as RE.

In this work, we achieved practical capacities in the range of ≈300-400 mAh·g^{-1} depending on the nitrogen content and upper cut-off potential, while previously reported capacity values of biomass-derived nitrogen-doped carbon range between ≈400 and 820 mAh·g^{-1} [60, 75-79]. It must be noted that a fair comparison of electrochemical data is difficult as carbon source, processing temperatures, nitrogen content and electrochemical protocols vary from one paper to the next. In particular, a lower cut-off potential close to 0V can result in lithium plating at the carbon electrode and increased capacity, but such conditions are unrealistic for practical applications. Our work is focused on the effect of nitrogen functionality on electrochemical properties, instead of looking for the best material with the highest possible reversible capacity.

3.2.2. Electrochemical investigations in pseudo full-cells and *post-mortem* XPS analysis

To avoid reactions occurring at the Li metal CE which may influence the performance in a half-cell setup, electrochemical investigations were also performed in pseudo full-cells, containing a capacity-oversized NCM-111 cathode in order to ensure that there is an excess of active lithium within the cell. **Figure 6-a** shows the long-term cycling stability experiments for 100 charge/discharge cycles at

186 $mA \cdot g^{-1}$ for the different anode materials (NCM-111 || carbon full-cell setup). The capacity retention after 100 cycles, in comparison to the capacity at the 4th cycle (first cycle after formation) amounts to 98, 77 and 78% for biomass:urea 1:0, 1:1 and 1:5 samples, respectively.

One of the often-disregarded limitations of doped carbon materials is the extremely poor 1st cycle C_{Eff}. Reported C_{Eff} values are far from those of commercial graphites which may achieve a first cycle C_{Eff} of ≥90-95% (according to graphite manufacturers). Values of only 39 ± 4% (biomass:urea 1:0), 40 ± 1% (biomass:urea 1:1), 41 ± 1% (biomass:urea 1:5) were achieved, likely as a result of the large BET specific surface area, surface heterogeneity and high chemical activity as a result of surface heteroatom groups [80]. A 1st cycle C_{Eff} of 50 % for the anode, using a realistic capacity balancing of ≈1.1:1 would lead to severe capacity fading after the first cycle due to significant consumption of active lithium from the cathode. Interestingly, an increase in the nitrogen content shows no evident influence on the 1st cycle $C_{Eff.}$

The evolution of the accumulated irreversible capacity (Q_{AIC}) [54] upon the long-term cycling experiments is shown in **Figure 6-b**. The curve of the undoped carbon electrode (biomass:urea 1:0) shows a small slope after the SEI formation cycles (3rd cycle) and slightly increases upon cycling due to a decrease in decomposition reactions, with a maximum Q_{AIC} value of 549 $mAh \cdot g^{-1}$ after 100 cycles. The Q_{AIC} values add up to 890 $mAh \cdot g^{-1}$ (biomass:urea 1:1) and 907 $mAh \cdot g^{-1}$ (biomass:urea 1:5) after 100 charge/discharge cycles. These large values indicate severe parasitic side reactions that might stem from the ongoing SEI formation and decomposition of electrolyte but can also be related to lithium trapping within the anode. The trend of the accumulated values in half-cells (shown in **Figure S5**, Supplementary data) correlates well with that observed in the pseudo full-cells, as especially the 1:5 samples show steadily increasing Q_{AIC} values.

Figure S9 shows representative potential profiles of different cycles during the long-term experiment (5th, 25th, 50th and 100th cycles) for the different anode materials. Previous investigations on the effect of nitrogen doping on Li diffusion by density functional theory simulations revealed that the strong Coulombic attraction between pyridinic/pyrrolic nitrogen and the adsorbed Li^+ may hinder the de-lithiation process [69]. Furthermore, *Machnikowski et al.* [81] reported that the Q_{irr} of nitrogen-doped carbon increased in a direct relation to the proportion of pyridinic groups. As pyridinic nitrogen atoms are located at the edge sites of graphene layers, they would act as active sites for electrolyte decomposition and solvated Li^+ trapping, resulting in an enhanced Q_{AIC} for the more doped samples.

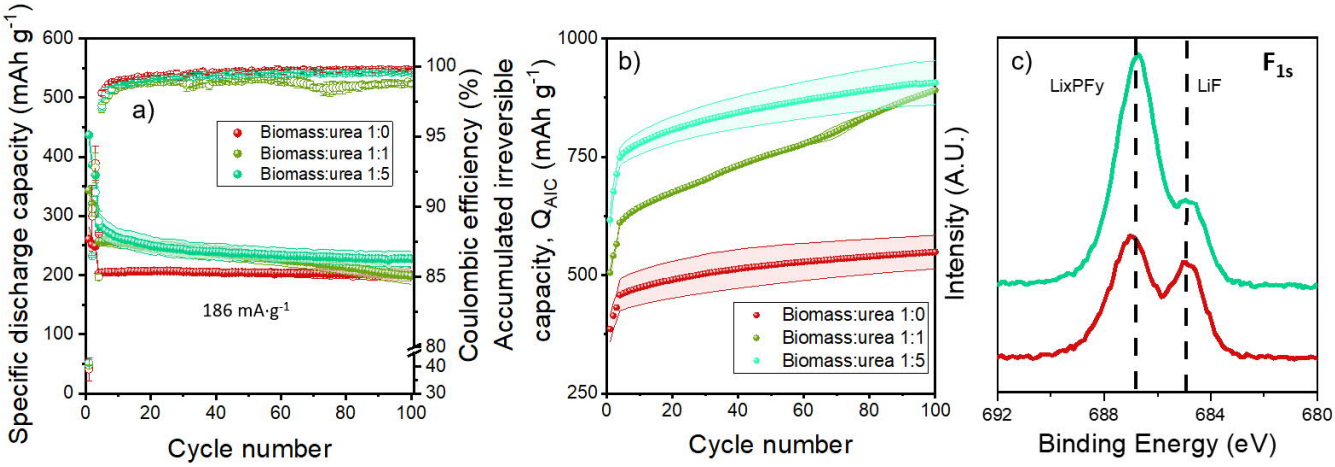

Figure 6. a) Cycling performance of carbonaceous anode materials at a specific current of 186 $mA \cdot g^{-1}$ for 100 cycles after three SEI formation cycles at 37.2 $mA \cdot g^{-1}$. b) Accumulated irreversible specific capacity *vs.* cycle number for constant current charge/discharge at 186 $mA \cdot g^{-1}$ during long-term cycling experiments. Pseudo full-cell setup: NCM-111 || carbon (N:P ratio 1:2.3) using Li metal as RE. Potential range of anode: 0.02-1.5 V *vs.* $Li|Li^+$. c) F_{1s} XPS core level spectra of the negative electrodes (biomass:urea 1:0 and 1:5) after cycling in NCM-111||carbon pseudo-full cells after 100 cycles.

Post-mortem XPS investigations of the cycled electrodes (after 100 cycles; biomass:urea 1:0 and 1:5) were performed in order to investigate changes in SEI formation and active lithium losses. Detailed core spectra and summary of atomic concentrations are included in the Supplementary data (**Figure S10**). It should be noted that the results from the cycled electrodes should not be compared with the XPS analysis of pristine electrodes as XPS is a surface sensitive technique (information depth ≈10 nm) and thus predominantly probes the SEI and not only the active material. The presence of more nitrogen functionality severely increases the amount of fluorine species from 9.5 (biomass:urea 1:0) to 13.6 (biomass:urea 1:5) at. % after 100 cycles, indicating further decomposition of $LiPF_6$. The relative amounts of carbon and oxygen do not significantly change between both electrodes. A slightly higher amount of Li is detected at the top layer of the biomass:urea 1:5 electrode, which indicates increased consumption of active Li. However, the relative concentration of Li estimated by XPS should not be directly correlated to the accumulated irreversible capacity (capacity loss) observed in the pseudo full-cells, because, as stated before, the analysis only elucidates ≈10 nm of the SEI.

The F_{1s} core level XPS spectra (**Figure 6-c**) shows two major components related to the formation of LiF and $Li_xPO_yF_z$ and/or Li_xPF_y phases resulting from the decomposition of the $LiPF_6$ salt [82]. For the electrode with a higher nitrogen content (biomass:urea 1:5; green curve), these two peaks exhibit a higher intensity in comparison to the undoped material (biomass:urea 1:0; red curve), indicating that

the addition of nitrogen enhances the decomposition of the conductive salt for the SEI formation. In the O_{1s} spectra (**Figure S10-b**), carbonaceous electrodes exhibit two overlapping peaks centered at 531.4 eV (C=O) and 533.6 eV (C-O) related to lithium alkyl carbonates and Li_2CO_3[83], respectively. As can be seen, the ratio of C=O to C-O is enhanced for the most doped sample, which could be related to a further contribution of Li_2CO_3.

Overall, further extensive electrochemical studies of capacity-balanced LIB full-cells and complementary analytical studies will be mandatory to clarify the mechanism of the enhanced irreversible capacities over cycling, *e.g.*, in order to distinguish between parasitic reactions due to SEI formation and irreversible lithium trapping [84].

4. Conclusions

In this work, the electrochemical properties of nitrogen-doped biomass-derived carbons as anode materials in LIB cells were critically discussed in terms of the nitrogen content. Nitrogen-doped carbons were synthetized by a ball-milling homogenization process of biomass resources and urea with different weight ratios, followed by heat-treatment under inert atmosphere. This two-step process allows for the incorporation of nitrogen homogeneously on the carbon particle surface, with atomic concentrations ranging between 0 and 12.7 at. % for biomass:urea 1:0 and 1:5 samples, respectively.

Based on our results, a higher nitrogen proportion results in an improved rate capability and enhanced maximum specific capacity as anode materials for LIB cells. However, these electrode materials suffer from disadvantages not frequently analyzed in the literature that may hinder their practical application. The energy efficiency (E_{Eff}), which means the ratio of input and output energies, decreased with increasing nitrogen content at the lowest current as a result of a large voltage hysteresis. E_{Eff} average values of ≈91% (biomass:urea 1:0), ≈87% (biomass:urea 1:1), ≈86% (biomass:urea 1:5) and ≈97 % (graphite) were reported. However, while non-doped carbons exhibited a declining trend in the E_{Eff} with increasing charge/discharge specific current, the E_{Eff} remained almost constant for the most doped sample up to 1860 $mA \cdot g^{-1}$. The working de-lithiation potential increased as a function of the nitrogen doping to almost 0.8 V *vs.* $Li|Li^+$. Unfortunately, this would result in a decreased cell voltage in a full-cell setup and, therefore, a decreased energy density of the cell.

Pseudo full-cell investigations using a capacity-oversized NCM-111 cathode with an excess of active Li revealed that the accumulated irreversible capacity continuously increased upon cycling for nitrogen-doped samples as a result of irreversible reactions. *Post-mortem* XPS analysis confirmed that

the high nitrogen content enhances further electrolyte decomposition and active Li losses in comparison to the undoped material.

With this analysis we emphasize that researchers should focus on the practical aspects such as voltage hysteresis, energy efficiency and Coulombic efficiency when considering novel anode materials. The application of nitrogen-doped carbons for applications requiring high-energy density would be strongly hindered as electrochemical properties are not competitive to those of graphite anodes despite the better rate capability. According with our results, these materials will be more suitable for high-power applications. Nevertheless, the large irreversibility of the storage reactions remains as a major drawback and needs to be tackled by improved material designs, *e.g.*, by reducing the large irreversible capacity in the first charge/discharge cycles.

Acknowledgements

The authors from University of Sevilla acknowledge funding by the Spanish Government Agency Ministerio de Economía y Competitividad under grant MAT2016-76526-R. SEM, TEM and textural characterization was performed at the CITIUS central services of the University of Seville (Spain). A. Gómez-Martín is grateful to the German Academic Exchange Service (DAAD) for funding her time at MEET under the "*Short-term research grants 2018*" program. The authors from University of Münster thank the MWIDE NRW for funding this work in the project "*GrEEn*" (funding code: 313-W044A). We are thankful to R. Nölle and L. Hanke for XPS measurements.

Captions

Figure 1. Representative SEM micrographs of a) biomass:urea 1:0 and b) biomass:urea 1:5 samples. c) Representative TEM micrograph of biomass:urea 1:5 sample. EDX elemental mappings of biomass:urea 1:5 sample (d) corresponding to e) C, f) N and g) O. h) Schematic structure of nitrogen-doped graphene monolayer. i) Results of N_{1s} spectra fitting of XPS analysis.

Figure 2. Rate capability of different anode materials: a) Specific discharge capacity *vs.* cycle number using specific charge/discharge currents between 37.2 and 7440 $mA \cdot g^{-1}$ and b) Capacity retention as a function of specific charge/discharge current, whereas the capacity at 37.2 $mA \cdot g^{-1}$ was defined as 100 % for each material. Error bars: standard deviation of three cells for each sample. Rate performance investigations: Cycles 1 - 3: 37.2 $mA \cdot g^{-1}$; Cycles 4 - 8: 372 $mA \cdot g^{-1}$; Cycles 9-59: specific currents of 37.2, 74.4, 186, 372, 744, 1166, 1860, 3720, 5580 and 7440 $mA \cdot g^{-1}$ for each step 5 cycles; Cycle 60 - onwards: 372 $mA \cdot g^{-1}$. Half-cell setup: carbon (WE)||Li metal (CE) cells using Li metal as RE. Potential range: 0.02 -1.5 V *vs*. $Li|Li^+$.

Figure 3. Evolution of a) E_{Eff}, b) C_{Eff} and c) V_{Eff} at different charge/discharge currents. Potential range: 0.02 V - 1.5 V *vs*. $Li|Li^+$. Half-cell setup: carbon (WE)||Li metal (CE) cells using Li metal as RE. Error bars: standard deviation of three cells for each sample. The red dashed area points out the range where nitrogen-doped samples maintain constant E_{Eff} and V_{Eff} despite the increase in specific current. The dashed arrow indicates the evolution of the trend for the biomass:urea 1:5 sample.

Figure 4. Representative potential as a function of the normalized capacity at a) 37.2 $mA \cdot g^{-1}$, b) 372 $mA \cdot g^{-1}$ and c) 1116 $mA \cdot g^{-1}$. The shadowed areas and arrows highlight the hysteresis between charge/discharge processes. Half-cell setup: carbon (WE)||Li metal (CE) cells using Li metal as RE.

Figure 5. a) Specific discharge capacities and b) representative potential profiles at different upper cut-off potentials from 1.5 to 3.0 V *vs*. $Li|Li^+$. Half-cell setup: carbon (WE)||Li metal (CE) cells using Li metal as RE.

Figure 6. a) Cycling performance of carbonaceous anode materials at a specific current of 186 mA·g-1 for 100 cycles after three SEI formation cycles at 37.2 mA·g-1. b) Accumulated irreversible specific capacity vs. cycle number for constant current charge/discharge at 186 mA·g-1 during long-term cycling experiments. Pseudo full-cell setup: NCM-111 || carbon (N:P ratio 1:2.3) using Li metal as RE. Potential range of anode: 0.02-1.5 V vs. Li|Li+. c) F_{1s} XPS core level spectra of the negative electrodes (biomass:urea 1:0 and 1:5) after cycling in NCM-111||carbon pseudo-full cells after 100 cycles.

Tables

Table 1. Summary of relevant structural properties, textural properties and surface chemistry[a] of nitrogen-doped carbon samples. [[a] The concentration of pyridinic, pyrrolic, graphitic, pyridinic oxide nitrogen (at. %) is normalized to the total nitrogen content of each sample]

Sample	BET specific surface area ($m^2 \cdot g^{-1}$)	I_{D_1} / I_G	Elemental composition (at. %) [a]						
			C	O	N Total	N pyridinic	N pyrrolic	N graphitic	N pyr-oxide
Biomass:urea 1:0	189.5	3.60	81.2	12.6	0	----	----	----	----
Biomass:urea 1:1	212.5	4.86	78.6	11.8	4.1	1.8	0.6	1.4	0.3
Biomass:urea 1:5	140.4	5.16	83.1	3.4	12.7	4.9	1.5	3.3	3.0

5. References

[1] Schmuch R, Wagner R, Hörpel G, Placke T, Winter M, Performance and cost of materials for lithium-based rechargeable automotive batteries, Nature Energy 2018; 3(4):267-78.

[2] Cano ZP, Banham D, Ye S, Hintennach A, Lu J, Fowler M, et al., Batteries and fuel cells for emerging electric vehicle markets, Nature Energy 2018; 3(4):279-89.

[3] Blomgren GE, The Development and Future of Lithium Ion Batteries, J Electrochem Soc 2017; 164(1):A5019-A25.

[4] Winter M, Barnett B, Xu K, Before Li Ion Batteries, Chem Rev 2018; 118(23):11433-56.

[5] Placke T, Kloepsch R, Dühnen S, Winter M, Lithium ion, lithium metal, and alternative rechargeable battery technologies: the odyssey for high energy density, J Solid State Electrochem 2017; 21(7):1939-64.

[6] Betz J, Bieker G, Meister P, Placke T, Winter M, Schmuch R, Theoretical versus Practical Energy: A Plea for More Transparency in the Energy Calculation of Different Rechargeable Battery Systems, Adv Energy Mater 2019; 9(6):1803170.

[7] Wagner R, Preschitschek N, Passerini S, Leker J, Winter M, Current research trends and prospects among the various materials and designs used in lithium-based batteries, J Appl Electrochem 2013; 43(5):481-96.

[8] Waldmann T, Hogg B-I, Wohlfahrt-Mehrens M, Li plating as unwanted side reaction in commercial Li-ion cells – A review, J Power Sources 2018; 384:107-24.

[9] Winter M, Möller K, Besenhard J, Carbonaceous and Graphitic Anodes, in: G.A. Nazri, G. Pistoia (Eds.), Science and technology of advanced lithium batteries: basic aspects, New York: Kluwer Academic Publishers2003, p. 50.

[10] Meister P, Jia H, Li J, Kloepsch R, Winter M, Placke T, Best Practice: Performance and Cost Evaluation of Lithium Ion Battery Active Materials with Special Emphasis on Energy Efficiency, Chem Mater 2016; 28(20):7203-17.

[11] Zhu B, Wang X, Yao P, Li J, Zhu J, Towards high energy density lithium battery anodes: silicon and lithium, Chem Sci 2019; 10(30):7132-48.

[12] Long W, Fang B, Ignaszak A, Wu Z, Wang Y-J, Wilkinson D, Biomass-derived nanostructured carbons and their composites as anode materials for lithium ion batteries, Chem Soc Rev 2017; 46(23):7176-90.

[13] Gomez-Martin A, Martinez-Fernandez J, Ruttert M, Heckmann A, Winter M, Placke T, et al., Iron-Catalyzed Graphitic Carbon Materials from Biomass Resources as Anodes for Lithium-Ion Batteries, ChemSusChem 2018; 11(16):2776-87.

[14] Holtstiege F, Koç T, Hundehege T, Siozios V, Winter M, Placke T, Toward High Power Batteries: Pre-lithiated Carbon Nanospheres as High Rate Anode Material for Lithium Ion Batteries, ACS Appl Energy Mater 2018; 1(8):4321-31.

[15] Al Hassan MR, Sen A, Zaman T, Mostari MS, Emergence of graphene as a promising anode material for rechargeable batteries: a review, Materials Today Chemistry 2019; 11:225-43.

[16] Zheng F, Yang Y, Chen Q, High lithium anodic performance of highly nitrogen-doped porous carbon prepared from a metal-organic framework, Nature Communications 2014; 5:5261.

[17] Wang J, Fan H, Shen Y, Li C, Wang G, Large-scale template-free synthesis of nitrogen-doped 3D carbon frameworks as low-cost ultra-long-life anodes for lithium-ion batteries, Chem Eng J 2019; 357:376-83.

[18] Wang X, Sun G, Routh P, Kim D-H, Huang W, Chen P, Heteroatom-doped graphene materials: syntheses, properties and applications, Chem Soc Rev 2014; 43(20):7067-98.

[19] Tian W, Li H, Qin B, Xu Y, Hao Y, Li Y, et al., Tuning the wettability of carbon nanotube arrays for efficient bifunctional catalysts and Zn–air batteries, J Mater Chem A 2017; 5(15):7103-10.

[20] Ma C, Shao X, Cao D, Nitrogen-doped graphene nanosheets as anode materials for lithium ion batteries: a first-principles study, J Mater Chem 2012; 22(18):8911-5.

[21] Zhang X, Zhu G, Wang M, Li J, Lu T, Pan L, Covalent-organic-frameworks derived N-doped porous carbon materials as anode for superior long-life cycling lithium and sodium ion batteries, Carbon 2017; 116:686-94.

[22] Yang Y, Jin S, Zhang Z, Du Z, Liu H, Yang J, et al., Nitrogen-Doped Hollow Carbon Nanospheres for High-Performance Li-Ion Batteries, ACS Appl Mater Interfaces 2017; 9(16):14180-6.

[23] Zheng C, Hu X, Sun X, Yoo SJ, Li X, Large-scale synthesis of nitrogen-rich hierarchically porous carbon as anode for lithium-ion batteries with high capacity and rate capability, Electrochim Acta 2019; 306:339-49.

[24] Tian L-L, Wei X-Y, Zhuang Q-C, Jiang C-H, Wu C, Ma G-Y, et al., Bottom-up synthesis of nitrogen-doped graphene sheets for ultrafast lithium storage, Nanoscale 2014; 6(11):6075-83.

[25] Yen P-J, Ilango PR, Chiang Y-C, Wu C-W, Hsu Y-C, Chueh Y-L, et al., Tunable nitrogen-doped graphene sheets produced with in situ electrochemical cathodic plasma at room temperature for lithium-ion batteries, Materials Today Energy 2019; 12:336-47.

[26] Bianco GV, Losurdo M, Giangregorio MM, Capezzuto P, Bruno G, Exploring and rationalising effective n-doping of large area CVD-graphene by NH3, PCCP 2014; 16(8):3632-9.

[27] Glerup M, Steinmetz J, Samaille D, Stéphan O, Enouz S, Loiseau A, et al., Synthesis of N-doped SWNT using the arc-discharge procedure, Chem Phys Lett 2004; 387(1):193-7.

[28] Senthilnathan J, Rao KS, Yoshimura M, Submerged liquid plasma – low energy synthesis of nitrogen-doped graphene for electrochemical applications, J Mater Chem A 2014; 2(10):3332-7.

[29] Ito Y, Christodoulou C, Nardi MV, Koch N, Sachdev H, Müllen K, Chemical Vapor Deposition of N-Doped Graphene and Carbon Films: The Role of Precursors and Gas Phase, ACS Nano 2014; 8(4):3337-46.

[30] Xing Z, Ju Z, Zhao Y, Wan J, Zhu Y, Qiang Y, et al., One-pot hydrothermal synthesis of Nitrogen-doped graphene as high-performance anode materials for lithium ion batteries, Scientific Reports 2016; 6:26146.

[31] Arif AF, Chikuchi Y, Balgis R, Ogi T, Okuyama K, Synthesis of nitrogen-functionalized macroporous carbon particles via spray pyrolysis of melamine-resin, RSC Advances 2016; 6(86):83421-8.

[32] Zheng F, Liu D, Xia G, Yang Y, Liu T, Wu M, et al., Biomass waste inspired nitrogen-doped porous carbon materials as high-performance anode for lithium-ion batteries, J Alloys Compd 2017; 693:1197-204.

[33] Soares OSGP, Rocha RP, Gonçalves AG, Figueiredo JL, Órfão JJM, Pereira MFR, Easy method to prepare N-doped carbon nanotubes by ball milling, Carbon 2015; 91:114-21.

[34] Schneidermann C, Jäckel N, Oswald S, Giebeler L, Presser V, Borchardt L, Solvent-Free Mechanochemical Synthesis of Nitrogen-Doped Nanoporous Carbon for Electrochemical Energy Storage, ChemSusChem 2017; 10(11):2416-24.

[35] Mondal AK, Kretschmer K, Zhao Y, Liu H, Fan H, Wang G, Naturally nitrogen doped porous carbon derived from waste shrimp shells for high-performance lithium ion batteries and supercapacitors, Microporous Mesoporous Mater 2017; 246:72-80.

[36] Jang J, Kim H-e, Kang S, Bang JH, Lee CS, Urea-assisted template-less synthesis of heavily nitrogen-doped hollow carbon fibers for the anode material of lithium-ion batteries, New J Chem 2019; 43(9):3821-8.

[37] Wang H, Zhang C, Liu Z, Wang L, Han P, Xu H, et al., Nitrogen-doped graphene nanosheets with excellent lithium storage properties, J Mater Chem 2011; 21(14):5430-4.

[38] Qie L, Chen W-M, Wang Z-H, Shao Q-G, Li X, Yuan L-X, et al., Nitrogen-Doped Porous Carbon Nanofiber Webs as Anodes for Lithium Ion Batteries with a Superhigh Capacity and Rate Capability, Adv Mater 2012; 24(15):2047-50.

[39] Hou J, Cao C, Idrees F, Ma X, Hierarchical Porous Nitrogen-Doped Carbon Nanosheets Derived from Silk for Ultrahigh-Capacity Battery Anodes and Supercapacitors, ACS Nano 2015; 9(3):2556-64.

[40] Shin WH, Jeong HM, Kim BG, Kang JK, Choi JW, Nitrogen-Doped Multiwall Carbon Nanotubes for Lithium Storage with Extremely High Capacity, Nano Lett 2012; 12(5):2283-8.

[41] Jeong M-G, Islam M, Du HL, Lee Y-S, Sun H-H, Choi W, et al., Nitrogen-doped Carbon Coated Porous Silicon as High Performance Anode Material for Lithium-Ion Batteries, Electrochim Acta 2016; 209:299-307.

[42] Ma L, Chen R, Hu Y, Zhu G, Chen T, Lu H, et al., Hierarchical porous nitrogen-rich carbon nanospheres with high and durable capabilities for lithium and sodium storage, Nanoscale 2016; 8(41):17911-8.

[43] Chen W, Wan M, Liu Q, Xiong X, Yu F, Huang Y, Heteroatom-Doped Carbon Materials: Synthesis, Mechanism, and Application for Sodium-Ion Batteries, Small Methods 2019; 3(4):1800323.

[44] Ji S, Imtiaz S, Sun D, Xin Y, Li Q, Huang T, et al., Coralline-Like N-Doped Hierarchically Porous Carbon Derived from Enteromorpha as a Host Matrix for Lithium-Sulfur Battery, Chem Eur 2017; 23(72):18208-15.

[45] Xia Q, Yang H, Wang M, Yang M, Guo Q, Wan L, et al., High Energy and High Power Lithium-Ion Capacitors Based on Boron and Nitrogen Dual-Doped 3D Carbon Nanofibers as Both Cathode and Anode, Adv Energy Mater 2017; 7(22):1701336.

[46] Gao C, Wang Q, Luo S, Wang Z, Zhang Y, Liu Y, et al., High performance potassium-ion battery anode based on biomorphic N-doped carbon derived from walnut septum, J Power Sources 2019; 415:165-71.

[47] Xu Y, Zhang C, Zhou M, Fu Q, Zhao C, Wu M, et al., Highly nitrogen doped carbon nanofibers with superior rate capability and cyclability for potassium ion batteries, Nature Communications 2018; 9(1):1720.

[48] Zhang H, Yang J, Hou H, Chen S, Yao H, Nitrogen-doped carbon paper with 3D porous structure as a flexible free-standing anode for lithium-ion batteries, Scientific Reports 2017; 7(1):7769.

[49] Winter M, Brodd RJ, What Are Batteries, Fuel Cells, and Supercapacitors?, Chem Rev 2004; 104(10):4245-70.

[50] Nölle R, Beltrop K, Holtstiege F, Kasnatscheew J, Placke T, Winter M, A reality check and tutorial on electrochemical characterization of battery cell materials: How to choose the appropriate cell setup, Mater Today 2020; 32:131-46.

[51] Winter M, The Solid Electrolyte Interphase – The Most Important and the Least Understood Solid Electrolyte in Rechargeable Li Batteries, Z Phys Chem 2009; 223(10):1395-406.

[52] Smith AJ, Burns JC, Trussler S, Dahn JR, Precision Measurements of the Coulombic Efficiency of Lithium-Ion Batteries and of Electrode Materials for Lithium-Ion Batteries, J Electrochem Soc 2010; 157(2):A196-A202.

[53] Winter M, Appel WK, Evers B, Hodal T, Möller K-C, Schneider I, et al., Studies on the Anode/Electrolyte Interfacein Lithium Ion Batteries, Monatshefte für Chemie / Chemical Monthly 2001; 132(4):473-86.

[54] Holtstiege F, Wilken A, Winter M, Placke T, Running out of lithium? A route to differentiate between capacity losses and active lithium losses in lithium-ion batteries, PCCP 2017; 19(38):25905-18.

[55] Gomez-Martin A, Martinez-Fernandez J, Ruttert M, Winter M, Placke T, Ramirez-Rico J, Correlation of Structure and Performance of Hard Carbons as Anodes for Sodium Ion Batteries, Chem Mater 2019.

[56] Vassilev SV, Baxter D, Andersen LK, Vassileva CG, Morgan TJ, An overview of the organic and inorganic phase composition of biomass, Fuel 2012; 94:1-33.

[57] Sarapuu A, Kibena-Põldsepp E, Borghei M, Tammeveski K, Electrocatalysis of oxygen reduction on heteroatom-doped nanocarbons and transition metal–nitrogen–carbon catalysts for alkaline membrane fuel cells, J Mater Chem A 2018; 6(3):776-804.

[58] Krüner B, Schreiber A, Tolosa A, Quade A, Badaczewski F, Pfaff T, et al., Nitrogen-containing novolac-derived carbon beads as electrode material for supercapacitors, Carbon 2018; 132:220-31.

[59] Kapteijn F, Moulijn JA, Matzner S, Boehm HP, The development of nitrogen functionality in model chars during gasification in CO2 and O2, Carbon 1999; 37(7):1143-50.

[60] An G-H, Kim H, Ahn H-J, Surface functionalization of nitrogen-doped carbon derived from protein as anode material for lithium storage, Appl Surf Sci 2019; 463:18-26.

[61] Bulusheva LG, Okotrub AV, Kinloch IA, Asanov IP, Kurenya AG, Kudashov AG, et al., Effect of nitrogen doping on Raman spectra of multi-walled carbon nanotubes, physica status solidi (b) 2008; 245(10):1971-4.

[62] Mao Y, Duan H, Xu B, Zhang L, Hu Y, Zhao C, et al., Lithium storage in nitrogen-rich mesoporous carbon materials, Energy Environ Sci 2012; 5(7):7950-5.

[63] Casco ME, Kirchhoff S, Leistenschneider D, Rauche M, Brunner E, Borchardt L, Mechanochemical synthesis of N-doped porous carbon at room temperature, Nanoscale 2019; 11(11):4712-8.

[64] Winter M, Novák P, Monnier A, Graphites for Lithium-Ion Cells: The Correlation of the First-Cycle Charge Loss with the Brunauer-Emmett-Teller Surface Area, J Electrochem Soc 1998; 145(2):428-36.

[65] Placke T, Siozios V, Schmitz R, Lux SF, Bieker P, Colle C, et al., Influence of graphite surface modifications on the ratio of basal plane to “non-basal plane” surface area and on the anode performance in lithium ion batteries, J Power Sources 2012; 200:83-91.

[66] Xiao M, Meng Y, Li Y, Liu X, Ke X, Ren G, et al., Tailoring nitrogen content in doped carbon by a facile synthesis with ionic liquid precursors for lithium ion batteries, Appl Surf Sci 2019; 494:532-9.

[67] Wu Z-S, Ren W, Xu L, Li F, Cheng H-M, Doped Graphene Sheets As Anode Materials with Superhigh Rate and Large Capacity for Lithium Ion Batteries, ACS Nano 2011; 5(7):5463-71.

[68] Hankel M, Ye D, Wang L, Searles DJ, Lithium and Sodium Storage on Graphitic Carbon Nitride, J Phys Chem C 2015; 119(38):21921-7.

[69] Das D, Kim S, Lee K-R, Singh AK, Li diffusion through doped and defected graphene, PCCP 2013; 15(36):15128-34.

[70] Lindström H, Södergren S, Solbrand A, Rensmo H, Hjelm J, Hagfeldt A, et al., Li+ Ion Insertion in TiO2 (Anatase). 2. Voltammetry on Nanoporous Films, J Phys Chem B 1997; 101(39):7717-22.

[71] Huggins RA, Negative Electrodes in Lithium Cells, Advanced Batteries: Materials Science Aspects, Springer US, Boston, MA, 2009, pp. 123-49.

[72] Jiang Z, Pei B, Manthiram A, Randomly stacked holey graphene anodes for lithium ion batteries with enhanced electrochemical performance, J Mater Chem A 2013; 1(26):7775-81.

[73] Hu T, Sun X, Sun H, Xin G, Shao D, Liu C, et al., Rapid synthesis of nitrogen-doped graphene for a lithium ion battery anode with excellent rate performance and super-long cyclic stability, PCCP 2014; 16(3):1060-6.

[74] Kasnatscheew J, Börner M, Streipert B, Meister P, Wagner R, Cekic Laskovic I, et al., Lithium ion battery cells under abusive discharge conditions: Electrode potential development and interactions between positive and negative electrode, J Power Sources 2017; 362:278-82.

[75] Wan H, Hu X, Nitrogen doped biomass-derived porous carbon as anode materials of lithium ion batteries, Solid State Ionics 2019; 341:115030.

[76] Kesavan T, Sasidharan M, Palm Spathe Derived N-Doped Carbon Nanosheets as a High Performance Electrode for Li-Ion Batteries and Supercapacitors, ACS Sustain Chem Eng 2019; 7(14):12160-9.

[77] Mondal AK, Kretschmer K, Zhao Y, Liu H, Wang C, Sun B, et al., Nitrogen-Doped Porous Carbon Nanosheets from Eco-Friendly Eucalyptus Leaves as High Performance Electrode Materials for Supercapacitors and Lithium Ion Batteries, Chem Eur 2017; 23(15):3683-90.

[78] Ou J, Yang L, Zhang Z, Xi X, Nitrogen-doped porous carbon derived from horn as an advanced anode material for sodium ion batteries, Microporous Mesoporous Mater 2017; 237:23-30.

[79] Wang B, Li S, Wu X, Liu J, Chen J, Biomass chitin-derived honeycomb-like nitrogen-doped carbon/graphene nanosheet networks for applications in efficient oxygen reduction and robust lithium storage, J Mater Chem A 2016; 4(30):11789-99.

[80] Jin J, Yu B-j, Shi Z-q, Wang C-y, Chong C-b, Lignin-based electrospun carbon nanofibrous webs as free-standing and binder-free electrodes for sodium ion batteries, J Power Sources 2014; 272:800-7.

[81] Machnikowski J, Grzyb B, Weber JV, Frackowiak E, Rouzaud JN, Béguin F, Structural and electrochemical characterisation of nitrogen enriched carbons produced by the co-pyrolysis of coal-tar pitch with polyacrylonitrile, Electrochim Acta 2004; 49(3):423-32.

[82] Niehoff P, Passerini S, Winter M, Interface Investigations of a Commercial Lithium Ion Battery Graphite Anode Material by Sputter Depth Profile X-ray Photoelectron Spectroscopy, Langmuir 2013; 29(19):5806-16.

[83] Michan AL, Parimalam BS, Leskes M, Kerber RN, Yoon T, Grey CP, et al., Fluoroethylene Carbonate and Vinylene Carbonate Reduction: Understanding Lithium-Ion Battery Electrolyte Additives and Solid Electrolyte Interphase Formation, Chem Mater 2016; 28(22):8149-59.

[84] Vortmann-Westhoven B, Winter M, Nowak S, Where is the lithium? Quantitative determination of the lithium distribution in lithium ion battery cells: Investigations on the influence of the temperature, the C-rate and the cell type, J Power Sources 2017; 346:63-70.